Adsorption/Desorption of Water and Ethanol on 3A Zeolite in Near-Adiabatic Fixed Bed

Marian Simo,* Siddharth Sivashanmugam, Christopher J. Brown,[†] and Vladimir Hlavacek

Department of Chemical and Biological Engineering, University at Buffalo, Buffalo, New York 14260

A pilot scale adsorber apparatus was designed and constructed to investigate water and ethanol adsorption/desorption kinetics on 3A zeolite for the design purposes of a fuel ethanol dehydration pressure swing adsorption (PSA) process. Equilibrium studies have shown that 3A zeolite adsorbed a significant amount of water while very weak ethanol adsorption was observed. The breakthrough curves were utilized to study the effects of column pressure, temperature, flow rate, pellet size, and adsorbate concentration on the overall mass transfer resistance. Based on experimentally observed trends, both macropore and micropore diffusion were identified as relevant mass transfer mechanisms. A mathematical model for a bench scale adsorption bed included the linear driving force (LDF) adsorption rate model and the variation of axial velocity. A detailed heat transfer model was a necessity since the bed dynamics was affected by heat transfer in the bed wall. The model was used to analyze the experimental data and extract values of pertaining diffusion coefficients.

Introduction

The use of ethanol for car fuel purposes has gained a wide popularity because of the fact that the raw material is renewable. A significant cost involved in the ethanol production process is the energy required for the product purification. The ethanol content of a fermentation broth is usually about 6−10 wt %. By simple distillation, the ethanol−water mixture can be enriched up to a maximum of 95 wt %. Further enrichment of ethanol must obviate the azeotropic point in order to deliver a fuel grade ethanol (≥99.5 wt %). Conventionally, the final purification was done by azeotropic distillation.[1] With the development of adsorption processes and invention of molecular sieves, pressure swing adsorption (PSA) replaced the azeotropic distillation process in the late 1980s.[2] The large scale process utilizes a 3A zeolite that preferentially adsorbs water while ethanol molecules are excluded. The PSA process is attractive due to the low energy consumption, its capability of producing very dry product, and its proven technical record.

In spite of the widespread application of this technology, a detailed numerical study on the operation and performance of this PSA process is not available. The quality of a PSA model largely depends on the accuracy of submodels used for the description of adsorption equilibrium, heat of adsorption, kinetics, and heat transfer dynamics. The coupling of these effects can be quite complicated in a real PSA process due to the fact that the operation is inherently transient.

The objective of this work was to study the adsorption/desorption kinetics of water and ethanol on a 3A zeolite in the range of operating conditions corresponding to the industrial ethanol dehydration PSA process. Dynamic breakthrough measurements in nonadiabatic fixed beds are a proven technique to assess the kinetic parameters for adsorption and desorption processes.[3,4] Adsorption breakthrough and desorption curves were measured at different operating conditions by varying the temperature, pressure, bed velocity, inlet concentration, and particle size. The effects of operating parameters were considered to formulate the adsorption/desorption kinetic model for

the diffusion in a 3A zeolite pellet. The unknown parameters were estimated by fitting experimental data to the postulated kinetic model. It was found that both macropore and micropore diffusion mechanisms are the controlling diffusion mechanisms.

Theory

Commercial zeolite adsorbents are made by compressing zeolite crystals (∼1 μm in diameter) into pellets (a few millimeters in diameter) with the aid of a binder. In general, the pellet uptake can be controlled by up to four distinct mass transfer resistances:[5] (1) An adsorbent particle is always enclosed by a laminar film separating the particle from the bulk fluid. (2) Macropores (voids in the pellet) act as a conduit to transport the gas molecules from the pellet surface to the particle interior. (3) Molecules are adsorbed on the surface of zeolite crystals (pore mouth), also known as the surface barrier resistance. (4) Eventually molecules diffuse within the zeolite crystal by a mechanism known as activated micropore diffusion. A combination of two diffusion mechanisms, Knudsen diffusion and the molecular (bulk) diffusion, is possible in the macropore region depending on the size of the pore and diffusing molecule.[5] Each of the above resistances exhibits a unique dependence on the operating conditions, and thus a carefully planned experiment can provide information on the rate-controlling mechanism.

There are only several citations in the open literature on the adsorption kinetics of water and ethanol on a 3A zeolite relevant to the ethanol−water PSA process. Several purely experimental studies have demonstrated the ability of a 3A zeolite to produce fuel grade ethanol in either liquid[6] or gaseous phase.[7,8] It was also concluded that the extent of the ethanol coadsorption is minimal; however, this claim was not supported quantitatively. Sowerby and Crittenden developed a kinetic model for ethanol drying in small columns for the purpose of a temperature swing adsorption (TSA) process design.[8] In their work, an ethanol−water vapor feed was used in dynamic nonisothermal breakthrough measurements. External fluid and solid film were considered as the relevant mass transfer resistances in the kinetic model. The range of experimental conditions was quite narrow, especially in terms of temperatures (105−120 °C), and the effect of pressure was not considered at all. The solid film coefficient, used to lump the adsorption rate inside the pellet, indicated the

---

* To whom correspondence should be addressed. E-mail: marian.simo@gmail.com.

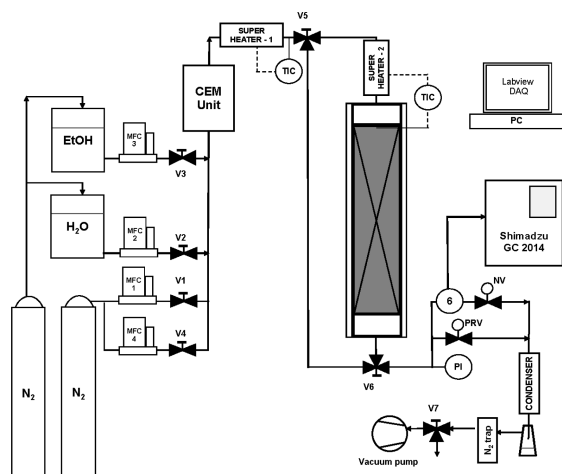† Thermal Kinetics Engineering PLLC, 2420 Sweet Home Road, Amherst, NY, 14228.

Figure 1. Simplified process flow sheet diagram of the kinetic apparatus. MFC, mass flow controller; TIC, temperature indicating controller; PRV, pressure regulating valve; PI, pressure indicator; NV, needle valve; 6, six port GC sampling valve.

importance of activated micropore diffusion since the system showed a strong temperature and concentration dependence. However, no comment on the actual mass transfer mechanism was made.

An isothermal breakthrough study for the ethanol−water mixture was performed by Kupiec et al.[7] Micropore diffusion was assumed to be the rate-limiting step; unfortunately diffusion coefficients were reported only at 100 °C. Studies of Sowerby and Kupiec used zeolite pellets of several millimeters in diameter.

Tian et al.[9] performed gravimetric temperature programmed desorption experiments with 3A zeolite particles smaller than 0.1 mm in diameter. It was assumed that the macropore and external film resistances were negligible for such small pellets. Micropore diffusion was considered as the sole mass transfer phenomenon governing the particle uptake. Data confirmed that the concentration and temperature dependences of the crystal diffusion coefficient conform to the Darken equation.

The Eigenberger group studied the breakthrough curves for water on W. R. Grace 4A zeolite.[10] They concluded that the macropore diffusion was the controlling mechanism. Experiments were conducted for temperatures from 25 to 80 °C and pressures from 2 to 5 bar. Both 3A and 4A pellets should be very similar in terms of their macropore structure; i.e., the same macropore diffusion mechanism should apply for both materials. However, it was not reported or observed experimentally that the macropore diffusion mechanism was relevant for adsorption uptake on a 3A zeolite.

Experimental Section

The dynamic breakthrough runs were performed to measure the equilibrium and kinetic parameters for water and ethanol on W. R. Grace 3A zeolite. The process flow sheet of the experimental apparatus is depicted in Figure 1. There are four elements that comprise the kinetic apparatus: (1) mixture preparation, (2) adsorber, (3) gas chromatograph, and (4) data acquisition.

(1) Mixture Preparation. Nitrogen, used as an inert carrier gas, was supplied from a pressure cylinder. The mass flow controller 1 (MFC) was used to control the nitrogen flow rate during adsorption and desorption experiments. The MFC 4 was used only for the bed regeneration. The MFCs 2 and 3 were used to control the flow of water and ethanol, respectively. Both

liquids were stored in two 4-gal tanks. An overpressure was created by compressed nitrogen in these tanks to force the flow of liquid toward the controlled evaporator mixer (CEM) unit. Any oscillations that would be normally introduced by a pump were thus eliminated. After the desired flows were set, liquid and gaseous streams were mixed in the CEM unit. The complete vapor generating system was supplied by Bronkhorst: water and ethanol MFCs LIQUI-FLOW L2302 series 10−500 g/h, nitrogen MFC EL-FLOW series 1−50 SLM (standard liters per minute), CEM unit (20−200 °C), and digital readout/control unit. The accuracy of MFCs was ±1% according to the manufacturer data. The temperature of the CEM generated vapor stream could be further adjusted by super heater 1. The three-way valves V5 and V6 were used to divert the stream to the bypass line or to the adsorber. A bypass line was used for gas chromatograph (GC) calibration or during a start-up of an experiment.

(2) Adsorber. A Swagelok 500 cm³ cylinder was used as the adsorber bed. The material of construction was 316 L stainless steel, the bed was 597 mm long, and the outside diameter was 48.2 mm with a 6.1 mm thick wall. At the top and at the bottom of the bed, 3.6 mm glass beads were used to ensure a proper gas distribution and stabilization of the zeolite layer. To ensure constant axial temperature profiles in the bed prior to an experimental run, the bed was equipped with six band heaters (∼200 W each) 76 mm long and 5 mm thick. A 110 mm thick layer of ceramic insulation was applied next to minimize the heat loss to the environment. Four thermocouple inserts were constructed to monitor axial temperatures at the bed positions: inlet, $L/3$, $2/3L$, and outlet. Each insert could hold up to three thermocouples (TC), so the temperatures in the radial direction could be tracked as well. The total number of TCs was eight due to the limitations of the data acquisition (DAQ) system. Omega K type TCs were used. W. R. Grace 3A zeolites 562ET (3.6 mm pellets) and 564ET (1.8 mm pellets) were used in the present study.

(3) Gas Chromatograph. A Shimadzu GC 2014 with a TCD detector was used for the monitoring of water, ethanol, and nitrogen concentrations. A necessary amount of vapor was bypassed into the GC sample loop to guarantee a stable and robust analysis. The flow rate was adjusted by a needle valve and was not measured. Two packed columns in series, Haysep D and Haysep Q, were used to obtain efficient and fast separation. The elution times at the GC column temperature 180 °C and helium (GC carrier gas) flow 50 mL/min were approximately 0.6, 1.2, and 3.5 min for nitrogen, water, and ethanol, respectively. The GC column lifetime was approximately 6 months for a constant operation.

(4) Data Acquisition. Constant monitoring of bed temperatures and pressure was achieved through a custom-made DAQ system. Labview was used to program necessary data acquisition and processing steps. A National Instruments Fieldpoint system was used for conditioning and digitalization of signals.

A Rosemount (high temperature) pressure indicator was installed right after valve V6 in Figure 1. A Swagelok pressure regulator was used to maintain isobaric operation during the experiment. In the next section of the apparatus, vapor was condensed and the liquid nitrogen cold trap was installed to prevent any contamination of the oil in the vacuum pump. Kinetic apparatus operating conditions were 100−200 °C and 2−6.7 bar pressure. All lines had to be isolated to prevent any vapor condensation. Electric heat tapes from Omega and ceramic insulation were used for this purpose.
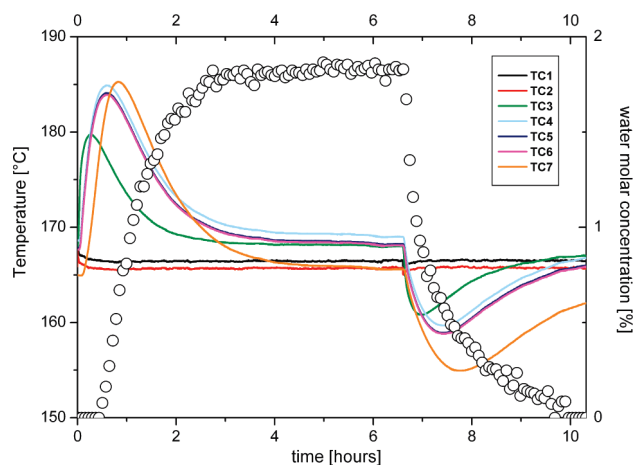
Figure 2. Experimental run w9. Temperature readings TC1 and TC2 correspond to the bed inlet, centerline, and wall values, respectively; TC3 corresponds to the centerline temperature at $L/3$ distance from the inlet; TC4, TC5, and TC6 correspond to the axial position at $2/3L$, centerline, midpoint, and wall, respectively; TC7 corresponds to the bed end centerline temperature.

Zeolite Regeneration. The zeolite bed was regenerated (or activated) for 12−20 h prior to each experiment. The regeneration conditions were the following: temperature in the range 220−240 °C, absolute pressure of 6−10 kPa, and nitrogen purge of 200 mL/min. Regeneration temperatures over 270 °C lead to an irreversible damage of the zeolite and a loss of the adsorbing capacity. Temperature in the bed was raised by changing the voltage of the band heaters using a variable transformer. After the activation was over, the power output was changed according to the desired experimental temperature. After the experimental pressure and nitrogen flow were adjusted, it took 4−6 h to obtain satisfactory initial bed temperature profiles.

Experiment. Each experimental run started with an activated bed that was exposed to a step change in the adsorbate concentration at time 0 h. The inlet concentration was kept constant by the Bronkhorst system. The effluent concentration, the bed pressure, and temperatures were constantly monitored until the bed was fully saturated with adsorbate and the initial temperature profiles were recovered. As the last step, the desorption run was started from the saturated bed condition.

A typical experimental run took approximately 15−30 h. It was inevitable to have a fully automatic DAQ and control system. First, the adsorption step was evaluated through the adsorbed component mass balance to obtain the corresponding equilibrium loading. Next, the adsorption breakthrough curve and the desorption curve were used in the evaluation of kinetic parameters. The raw experimental data for a typical experimental run are shown in Figure 2.

Mathematical Model

Mathematical models for adsorption column dynamics of different complexities have been introduced.[11] The simplest breakthrough model is an isothermal plug flow model with trace level concentration of adsorbing component and linear isotherm. For adsorption of water on a 3A zeolite a more complex model is necessary; see Table 1. A nonisothermal model is required because of the high heat of adsorption. In addition, a high water concentration ($\geq 10\%$) is required to treat the problem as a bulk separation. Heat effects and the variation of the bed velocity must be considered.

A detailed derivation of the model can be found elsewhere.[11,12] An axially dispersed plug flow model was assumed for both mass and heat transfer processes in the bed and the absence of radial bed profiles since $L/D > 10$. Experiments were conducted at low pressures; thus ideal gas behavior was assumed. The fixed bed adsorber was equipped with a pressure controller at the bed outlet; as a result, an isobaric operation was assumed since the pressure drop is not significant for a short bed. Variation of the axial velocity was accounted for through the overall mass balance.

A separate energy balance for the gas and solid phase was considered. Temperature gradients within the pellet were neglected; heat transfer from the pellet was entirely due to the fluid film resistance.[11] The adsorber wall energy balance was also included in the model since it was experimentally observed that the accumulation of heat in the bed wall affected the column dynamics.

Axial dispersion terms for component mass balance and gas phase heat balance had little effect on the concentration and temperature history. Since the isotherm was highly nonlinear for our system, steep temperature and concentration profiles were expected. In order to make the numerical scheme more stable, axial dispersion terms were fully accounted for, even though the corresponding Peclet numbers were in the range 300−600.

The zeolite pellet uptake model (adsorption rate) can be substantially simplified by introducing the linear driving force (LDF) approximation as suggested by Glueckauf.[13] Two partial differential equations describing the mass transfer rates in the pellet and zeolite crystals are replaced by a single ordinary differential equation. The success and wide application of the LDF model in the adsorption modeling is due to its physical consistency and tremendous savings in computational time compared to detailed pore models.[14]

For particles with bidispersed pore structure, the overall mass transfer coefficient k_{LDF} can be approximated by the series combination of resistances as

$$\frac{1}{k_{LDF}} = \frac{\Lambda R_P}{3(1-\varepsilon_B)k_f} + \frac{\Lambda R_P^2}{15(1-\varepsilon_B)\varepsilon_P D_p} + \frac{r_c^2}{15 D_c} \quad (7)$$

Thus the overall resistance is composed of contributions from the external film, macropore region, and micropore region, respectively.[3,10] The partition ratio Λ is defined by eq 8.

$$\Lambda = \frac{\rho_B q_{ref}}{c_{ref}} \quad (8)$$

The micropore diffusion coefficient shows a significant temperature and concentration dependence usually expressed by the Darken equation, eq 9. The concentration dependent term can be evaluated from an equilibrium isotherm. The temperature dependence of self-diffusion coefficient (or corrected diffusivity, D_0) is usually correlated through eq 10.[5]

$$D_c = D_0 \frac{d \ln P}{d \ln q}_T \quad (9)$$

$$D_0 = D_\infty \exp\left(-\frac{E_a}{RT}\right) \quad (10)$$

In order to maintain constant initial temperature profiles, the bed was equipped with band heaters and only then a layer of insulation was applied. Thus the temperature of the wall was locally affected by heat input from the band heaters, conduction

Table 1. Mathematical Model of Isobaric Nonisothermal Fixed Bed Adsorber with Initial and Boundary Conditions

	Eq.	Initial Conditions (t=0)	Boundary Conditions (t>0)
Component Mass Balance: $$\frac{\partial Y_1}{\partial t} = D_L \frac{\partial^2 Y_1}{\partial z^2} - \frac{u}{\varepsilon}\frac{\partial Y_1}{\partial z} - \frac{\rho_B}{\varepsilon}\frac{RT_g}{P}(1-Y_1)\frac{\partial \bar{q}}{\partial t}$$	(1)	$\forall z \quad Y_1 = 0$	$z=0 \quad \varepsilon D_L \left.\frac{\partial Y_1}{\partial z}\right|_{z=0} = u\left(Y_1\big|_{z=0} - Y_{1,F}\right)$ $z=L \quad \left.\frac{\partial Y_1}{\partial z}\right|_{z=L} = 0$
Overall Mass Balance: $$\frac{\partial u}{\partial z} = \frac{u}{T_g}\frac{\partial T_g}{\partial z} - \rho_B \frac{RT_g}{P}\frac{\partial \bar{q}}{\partial t}$$	(2)	$\forall z \quad u = u_F$	$z=0 \quad u = u_F$
Adsorption Rate: $$\frac{\partial \bar{q}}{\partial t} = k_{LDF}\left(q^*(P_1, T_s) - \bar{q}\right)$$	(3)	$\forall z \quad \bar{q} = 0$	
Energy Balance for Fluid Phase: $$\rho_g c_{p_g}\frac{\partial T_g}{\partial t} = \lambda_L \frac{\partial^2 T_g}{\partial z^2} - \frac{u}{\varepsilon}\rho_g c_{p_g}\frac{\partial T_g}{\partial z} + \frac{(1-\varepsilon)}{\varepsilon}\frac{3h_{fs}}{R_p}(T_s - T_g) + \frac{4h_w}{\varepsilon D_1}(T_w - T_g)$$	(4)	$\forall z \quad T_g = T_F$	$z=0 \quad \varepsilon \lambda_L \left.\frac{\partial T_g}{\partial z}\right|_{z=0} = \rho_g C_{pg}u\left(T_g\big|_{z=0} - T_F\right)$ $z=L \quad \left.\frac{\partial T_g}{\partial z}\right|_{z=L} = 0$
Energy Balance for Pellet: $$\rho_P\left(C_{ps} + C_{p,1}\bar{q}\right)\frac{\partial T_s}{\partial t} = (-\Delta H)\rho_P\frac{\partial \bar{q}}{\partial t} + \frac{3h_{fs}}{R_P}(T_g - T_s)$$	(5)	$\forall z \quad T_S = T_F$	
Energy Balance for Wall: $$\rho_w c_{pw}\frac{\partial T_w}{\partial t} = \lambda_w \frac{\partial^2 T_w}{\partial z^2} + \frac{4h_w D_1(T_g - T_w) - 4h_e D_2(T_w - T_a)}{(D_2^2 - D_1^2)} + \frac{4Q_L}{\pi(D_2^2 - D_1^2)}$$	(6)	$\forall z \quad T_w = T_F$	$z=0 \quad \left.\frac{\partial T_w}{\partial z}\right|_{z=0} = 0$ $z=L \quad \left.\frac{\partial T_w}{\partial z}\right|_{z=L} = 0$

in the bed wall, heat transfer through the bed wall from the zeolite bed, and heat transfer through the insulation to the environment. By considering such a detailed model, two additional parameters were introduced—heat transfer coefficient at the wall h_w and the external heat transfer coefficient h_e—lumping the thermal resistance of the insulation and the thermal resistance due to the natural convection heat transfer outside the adsorber.

The set of partial differential equations reported in Table 1 was solved by the method of lines using standard initial and boundary conditions. Initially an adsorbate free bed was assumed for adsorption, while the saturated bed initial conditions for gas and solid concentrations were used for the desorption modeling. The discretization approximation in the axial direction by five point upwind finite differences[15] resulted in the system of ordinary differential/algebraic equations (DAEs). Fifty axial points were required to obtain a reasonable level of accuracy and stability. The maximum time step of 1 s was used in all calculations. The modeling of adsorption systems with a nonlinear isotherm produces a set of stiff DAEs; hence, they were solved by the DASSL code designed by Petzold[16] using an implicit backward differentiation formula. The FORTRAN IMSL Library subroutine DDASPG, based on DASSL, was used to solve the problem in double precision arithmetic on a standard laptop 1.6 GHz computer.

Estimation of Model Parameters

The parameters in eqs 1–7 were either measured or determined from empirical correlations. The axial dispersion coefficient, D_L, was determined by the correlation suggested by Wakao and recommended by Ruthven:[11]

$$\frac{D_L}{ud_p} = \frac{20}{Sc\ Re} + \frac{1}{2} \tag{11}$$

The fluid phase axial thermal conductivity, λ_L, was estimated by the correlation given by Dixon:[17]

$$\frac{1}{Pe_{AF}} = \frac{0.73\varepsilon_B}{Re\ Pr} + \frac{0.5}{1 + \dfrac{9.7\varepsilon_B}{Re\ Pr}} \tag{12}$$

The fluid film mass transfer coefficient was estimated from the correlation (13) given by Wakao and Funazkri.[18] The correlation is valid for a wide range of Reynolds numbers in the range $3 < Re_P < 10^4$. The fluid−solid (particle) heat transfer coefficient, h_{fs}, was obtained by assuming an analogy between mass and heat transfer; the corresponding coefficient was estimated from eq 14. The procedure was used with success in the adsorption modeling at high Reynolds numbers.[11]

$$Sh = 2.0 + 1.1Sc^{1/3}Re^{0.6} \tag{13}$$

$$Nu = 2.0 + 1.1Pr^{1/3}Re^{0.6} \tag{14}$$

Physical and transport properties such as gas viscosity, thermal conductivity, and specific heat capacity were calculated for a mixture of water or ethanol in the nitrogen carrier according to generally accepted formulas and property correlations.[19] All important system characteristics are summarized in Table 2.

The value of the volumetric heat source output Q_L in eq 6 was evaluated from the initial conditions. Since the power output of all band heaters was kept constant throughout the experiment and all other parameters were already known, the value for Q_L was estimated from the initial temperature profiles in the bed with the aid of mathematical model.

The external heat transfer coefficient, h_e, was introduced by considering a rigorous energy balance for the adsorber wall. The value of the coefficient h_e was determined experimentally

Table 2. Column and Adsorbent Characteristics

Column	
adsorbent layer length, L	0.518 m
internal diameter, D_1	0.034 m
outer diameter, D_2	0.058 m
external diameter, D_3	0.165 m
bed void fraction, ε_B	0.36
bulk density, ρ_B	770 kg/m³
Wall (316 SS)	
density, ρ_w	8000 kg/m³
heat capacity, $c_{p,w}$	500 J·kg⁻¹·K⁻¹
thermal conductivity, λ_w	17 W·m⁻¹·K⁻¹
Adsorbent: W. R.Grace 3A Zeolite	
pellet density, ρ_P	1199.3 kg/m³
adsorbent particle radius, R_P	1.785×10^{-3} m
pellet porosity, ε_P	0.37
BET surface area	45 m²/g
pellet thermal conductivity, λ_P	0.12 W·m⁻¹·K⁻¹
pellet heat capacity, $c_{p,s}$	1045 J·kg⁻¹·K⁻¹

by heating the initially cold bed with the carrier gas (band heaters were turned off) until steady state was reached.

$$Nu_w = 0.2Pr^{1/3}Re^{0.8} \qquad (15)$$

Small radial temperature gradients in the bed (1−2 °C) indicated that the major heat transfer resistance was in the insulation and thus only an order of magnitude estimate for h_w was necessary. The value of the wall heat transfer coefficient, h_w, did not have a significant effect on the generated temperature curves. This was expected because of the large difference in thermal conductivities of the steel wall and ceramic wool insulation and turbulent flow conditions inside the bed. The correlation given by Dixon, eq 15, was used to obtain an estimate for the wall heat transfer coefficient.[17] The developed model was used to estimate the heat transfer coefficient for various flows and temperatures. The values of the parameter h_e showed only a weak dependence on the temperature and flow rate, as can be seen from Figure 3.

Results and Discussion

Equilibrium Data. The adsorption breakthrough runs were used to obtain equilibrium data for adsorbing components. Initially clean bed was exposed to a step input of the adsorbate
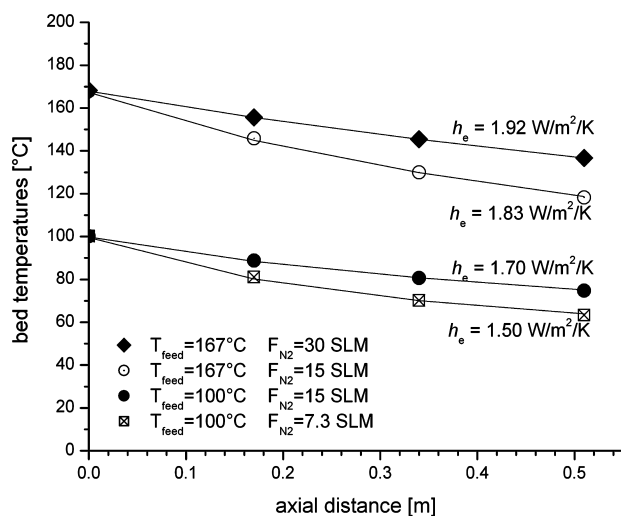
Figure 3. Comparison of experimental (points) and calculated (lines) temperature profiles used for estimation of external heat transfer coefficient h_e for temperatures 100 and 167 °C and flows of 7.3, 15, and 30 SLM.
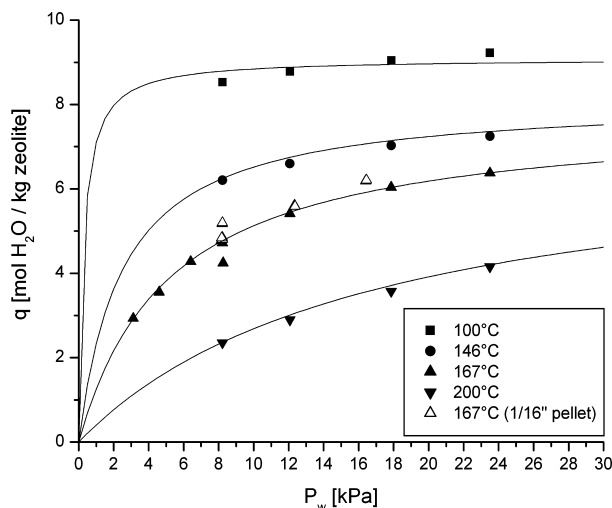
Figure 4. Equilibrium isotherms of water vapor on 3A zeolite. Data were measured at 100, 146, 167, and 200 °C for 3.6 mm pellets and at 167 °C for 1.8 mm pellets. Solid lines represent the fit with the Langmuir isotherm model.

Table 3. Langmuir Equilibrium Model and Parameters for Water on 3A Zeolite

$q_w{}^* = q_{s,w}(T)\dfrac{b(T)P_w}{1 + b(T)P_w}$	$b_\infty = 5.3126 \times 10^{-10}$ K⁰·⁵ Pa⁻¹; $\gamma = 23.235 = Q_{st}/R/T_0$; $q_{0,w} = 10.7446$ mol/kg; $\delta = 0.687\,92$; $T_0 = 300$ K
$b(T) = \dfrac{b_\infty}{\sqrt{T}} \exp\left(\gamma\dfrac{T_0}{T}\right)$	
$q_{s,w}(T) = q_{0,w} \exp\left(\delta\left(1 - \dfrac{T}{T_0}\right)\right)$	

concentration, and after reaching the equilibrium, the adsorbate uptake was evaluated through the overall mass balance.

Figure 4 shows adsorption isotherms for water vapor obtained at 100, 146, 167, and 200 °C on a 3A zeolite for particle diameters 3.6 and 1.8 mm, respectively. The parameters of the equilibrium model were obtained by a nonlinear least-squares optimizer from MATLAB. The Langmuir model with the temperature dependent saturation capacity q_s proved adequate. The values of the model parameters are summarized in Table 3.

The isosteric heat of adsorption for the system water−3A zeolite was evaluated from the value of parameter γ (see Table 3) to be 57.95 kJ/mol. Sowerby[8] and Carmo[20] used the values 50 and 43 kJ/mol. Lalik et al. have measured the heat of adsorption of water on a 3A zeolite in the range 57−72 kJ/mol in a microcalorimetric study.[21] Gorbach's work with a 4A zeolite assumed 54.9 kJ/mol.[10]

The ethanol uptake by a 3A zeolite was studied at temperatures 100, 146, and 167 °C, respectively. The experimental run carried out at 167 °C is shown in Figure 5. An immediate breakthrough was observed, indicating a very low bed capacity for ethanol.

Equilibrium loading of 0.03 mol/kg was obtained for the first step in the experimental run E3. A very low ethanol loading can be predicted from the temperature profiles as well. A slight temperature increase can be observed for the first step only, indicating that all sites available for ethanol adsorption were occupied and no further adsorption takes place in the following steps. The fact that the small exothermic spike for the first step

Table 4. Experimental Conditions, Fitted k_{LDF} Values, and Mass Transfer Resistances

									resistance [s]		
run no.	P [kPa]	T [°C]	u_s [m/s]	P_{H_2O} [kPa]	F_{N_2} [SLM]	F_{H_2O} [g/h]	d_P [mm]	$10^3 k_{LDF}$ [s^{-1}]	external film	macropore	micropore
w1	448	146	0.078	8.2	15	13.5	3.57	0.90	51	376	685
			0.083	34.3	15	60	3.57	0.90	15	13	1084
w2	448	100	0.083	8.2	15	13.5	3.57	0.55	73	605	1140
			0.083	23.5	15	40	3.57	0.55	N/A	N/A	N/A
w3	448	200	0.088	8.2	15	13.5	3.57	8.50	18	100	0
			0.086	23.5	15	40	3.57	8.50	11	58	48
w4	448	167	0.083	8.2	15	13.5	3.57	1.90	37	259	230
			0.082	23.5	15	40	3.57	1.90	17	67	442
w5	224	167	0.083	8.2	7.35	13.5	3.57	2.60	26	130	229
			0.08	8.2	7.35	13.5	3.57	2.60	26	96	262
w6	689	167	0.083	8.2	23.2	13.5	3.57	1.50	46	399	222
			0.082	8.2	23.2	13.5	3.57	1.50	46	297	324
w7	448	167	0.083	12.3	15	20.5	3.57	2.00	28	202	269
			0.082	12.3	15	20.5	3.57	2.00	28	136	336
w8	448	167	0.085	16.4	15	27.5	3.57	2.30	23	167	245
			0.082	16.4	15	27.5	3.57	2.30	23	102	310
w9	448	167	0.167	8.2	30	27	3.57	2.20	26	259	169
			0.163	8.2	30	27	3.57	2.20	26	193	236
w10	448	167	0.218	3.1	40	13.5	3.57	1.95	36	399	77
			0.221	8.2	40	36	3.57	1.90	22	193	311
w11	448	167	0.083	8.2	15	13.5	1.785	9.5	12	65	28
			0.082	8.2	15	13.5	1.785	9.5	12	48	45
w12	689	167	0.083	8.2	23.5	13.5	1.785	5.5	15	102	65
			0.082	8.2	23.5	13.5	1.785	5.8	15	74	83
w13	448	167	0.083	12.3	15	20.5	1.785	10.5	9	51	35
			0.082	12.3	15	20.5	1.785	10.5	9	34	52
w14	448	167	0.085	16.4	15	27.5	1.785	11.5	7	42	38
			0.082	16.4	15	27.5	1.785	11.5	7	25	54
w15	448	167	0.167	8.2	30	27	1.785	8.5	9	68	41
			0.163	8.2	30	27	1.785	8.3	9	48	63

can be compared with the endothermic peak accompanying final desorption stage leads to the same conclusion.

The adsorbent selectivity for the ethanol−water mixture can be now evaluated for the PSA feed stream conditions—92 wt % ethanol, 167 °C, 448.2 kPa—using the experimental value for the ethanol and water equilibrium model from Table 3. The value of ∼900 for the adsorbent selectivity (analogue to relative volatility in distillation) illustrates the molecular sieving mechanism for ethanol−water separation by the PSA process.

Water Adsorption Kinetics Study. Breakthrough experiments were carried out to study the effect of the temperature, pressure, water concentration, flow rate, and pellet size on the bed performance and on the adsorption/desorption kinetics. The experimental apparatus and procedure were discussed earlier. Adsorption and desorption steps were performed in sequence for each experimental run. Table 4 summarizes all performed experiments; here conditions for adsorption are always shown first.
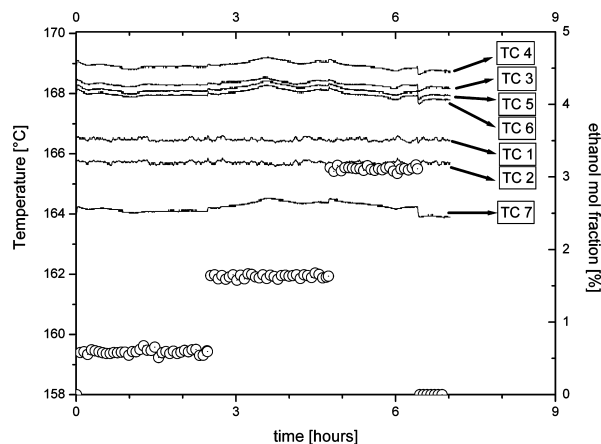
A typical adsorption run is depicted in Figure 6, where the water breakthrough occurred after 1.25 h. The slope of the breakthrough curve, especially in the early stage, is proportional to the adsorption rate. The steeper the curve the higher is the value of the mass transfer coefficient. An infinite value of the mass transfer coefficient would lead to a shock front and maximum bed utilization (dashed line in Figure 6). Mass transfer has thus a negative dispersive effect on the column performance.

The shape of the concentration breakthrough curve is point-symmetric to the center of the front for an isothermal system with a linear equilibrium isotherm; both conditions are strongly violated in the case of water adsorption on a 3A zeolite. The effect of the isotherm shape was positive for adsorption since for a favorable isotherm a fixed bed transition approaches a
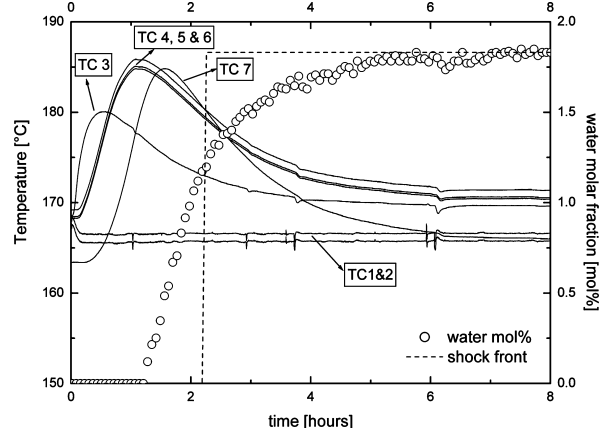

Figure 5. Ethanol breakthrough run E3. Operating conditions: 167 °C, 448.2 kPa, F_{N_2} = 20 SLM, ethanol flow rate 13.5, 40, and 80 g/h, respectively.

Figure 6. Effluent concentration history (right axis) and bed temperature profiles (left axis) for experimental run w4, adsorption step. Temperature readings at four axial positions: at $z = 0$ TC 1& 2 correspond to centerline and wall values, respectively; TC 3 corresponds to the centerline temperature at $L/3$; at $z = 2/3$ L TC 4, 5 & 6 correspond to centerline, midpoint, and wall values, respectively; TC 7 corresponds to the bed end centerline temperature.
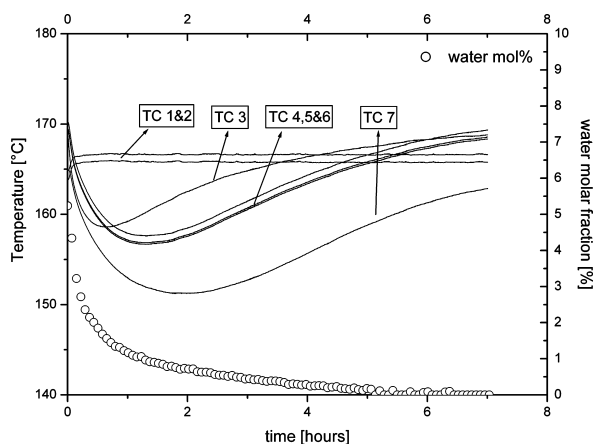
Figure 7. Effluent concentration history (right axis) and bed temperature profiles (left axis) for experimental run w4, desorption step. Temperature readings at four axial positions: at $z = 0$ TC 1 & 2 correspond to centerline and wall values, respectively; TC 3 corresponds to the centerline temperature at $L/3$; at $z = 2/3L$ TC 4, 5 & 6 correspond to centerline, midpoint and wall values, respectively; TC 7 corresponds to the bed end centerline temperature.

constant pattern profile.[22] The symmetry of the breakthrough curve was disturbed mostly by the heat effects. An increase of the temperature decreases the solid phase equilibrium loading, and even after the front had passed, the bed remained hot. As a result, the approach to the equilibrium in the later part of the breakthrough curve was controlled by heat transfer, i.e., by cooling of the bed. The cooling of the bed is usually a slower process. It can be due to the heat transfer rate in the laminar film surrounding the particle or due to the magnitude of heat convection in the bed given by the carrier gas and adsorbent heat capacities. The bed always heats up faster than it cools down due to the fact that the heat is generated inside the particle while the cooling rate is governed by phenomena occurring outside the particle.

As can be seen in Figure 6, the temperature profiles were not developed immediately and it took approximately 2/3 of the bed length. It is important to mention here that any flow nonidealities could be responsible for further complications. A detailed analysis of dynamic interactions due to the adsorption kinetics as well as the coupling of heat and mass transfer will be addressed separately in the modeling section.

In the case of desorption, the effect of isotherm was undesirable because an unfavorable isotherm generates a spreading or dispersive profile. A typical desorption run with the characteristic spreading concentration profile is depicted in Figure 7. In the early stage, the desorption process was fast because the water concentration was high and so was the bed temperature. The rate of desorption depends on the driving force and the mass transfer coefficient and both are decreasing as the desorption progresses; in addition the isotherm becomes more unfavorable.

The heat effects were smaller in the desorption operation compared to the adsorption due to the dispersive effect of an unfavorable isotherm. Since desorption is an endothermic process, the temperature should be increased in order to speed up the process. Heat was supplied to the system only by the feed stream, and nitrogen has a low thermal capacity compared to the heat capacity of the solid matrix. Several experimental studies have pointed out that the increase in the carrier gas flow rate had a positive effect on the course of desorption.[23] This can be explained by improved mass and heat transfer coefficients as well as by increased heat supply to the system.

Effect of Temperature. The effect of the bed temperature was investigated in the experimental runs w1, w2, w3, and w4. Figure
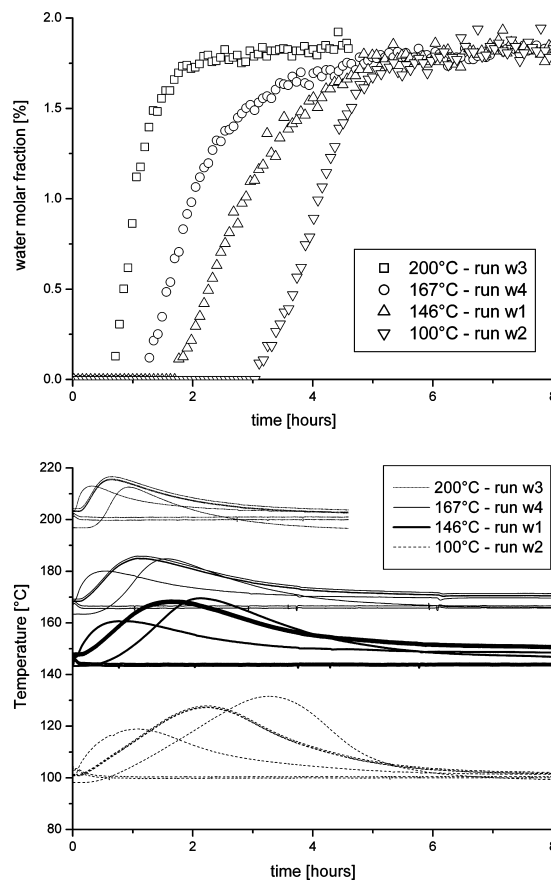

Figure 8. Adsorption breakthrough curves of water on 3A zeolite at 200, 167, 146, and 100 °C, respectively (top). Temperature profiles at four axial positions at the bed inlet, $L/3$, $2/3L$, and the bed end (bottom).

8 depicts the adsorption breakthrough curves and the temperature profiles for bed temperatures of 200, 167, 146, and 100 °C, respectively. All other parameters were kept constant; see Table 4.

The breakthrough time decreased with the increasing temperature owing to the decrease in the bed capacity. The breakthrough times of 0.65, 1.18, 1.68, and 3.1 h were observed as the temperature decreased. An increasing trend of the slope of the breakthrough curve can be observed with an increase of the temperature. This strong temperature dependence can be explained by the presence of the micropore diffusion mechanism. While the diffusion coefficients for pore diffusion (bulk and Knudsen) have only a weak temperature dependence, a strong temperature dependence is typical for activated micropore diffusion inside the zeolite crystals.

The amount of water adsorbed increased when the temperature decreased; as a consequence, more heat was generated during the adsorption. This fact can be extracted from the evolution of temperature profiles. In other words, the temperature rise $\Delta T = (T_{max} - T_{inlet})$ or hot spot increased with a decrease of the temperature. The temperature rise in the bed at 200 °C was only 15 K, while for 100 °C a temperature rise of 35 K was observed.

Similar trends are anticipated during the desorption process; see Figure 9. At 200 °C, the water amount adsorbed was low and, as a result, the bed was regenerated in less than 4 h. The equilibrium isotherm was almost linear at elevated temperatures (Figure 4), and thus the isotherm effect did not play any significant role. At lower temperatures, the zeolite adsorption capacity for water increased; the isotherm became more unfavorable and desorption profiles were more dispersed. The water concentration dropped below a detectable limit after ~5 h for the experimental run at
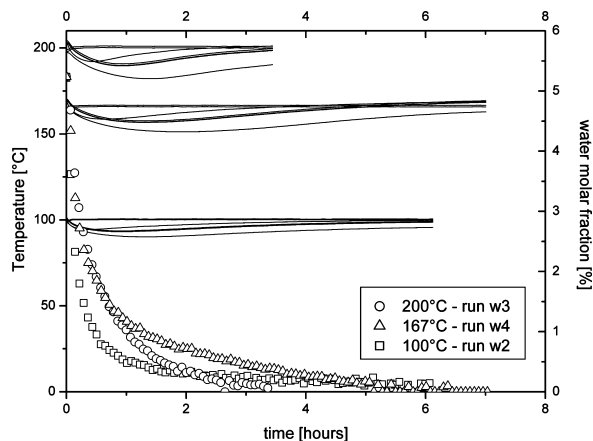
Figure 9. Temperature and concentration profiles for water desorption on 3A zeolite for bed temperatures of 200, 167, and 100 °C, respectively. Temperatures were measured at four different locations: the bed inlet, $L/3$, $2/3L$, and the bed end.
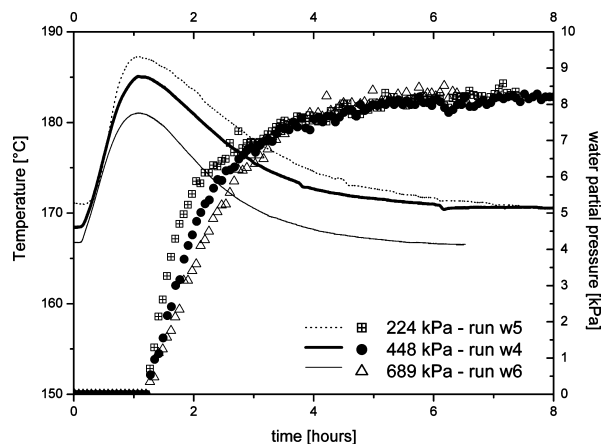

Figure 10. Temperature and concentration profiles for water adsorption on 3A zeolite for pressures 224, 448, and 689 kPa, respectively. Temperature at axial position of $2/3L$ is shown. Pellet size was 3.6 mm.

167 °C; however, for the experiment at 100 °C water was still present even after 6 h of regeneration.

Effect of Pressure. The individual mass transfer resistances for an adsorbent with bidisperse pore structure such as zeolite are external laminar film, macropore resistance, and diffusion in the zeolite crystals (micropores). Among these only the rate of diffusion in macropores is affected by the pressure. Experimental runs w4, w5, and w6 were carried out to confirm or contradict the significance of the macropore resistance. Figure 10 depicts the measured concentration and temperature profiles.

It is evident that the slope of the breakthrough curve increased as the pressure decreased. An increase of the rate of adsorption can be realized from the temperature profiles as well. The hot spot increased for lower pressures. It follows that the mass transfer into the pellet must be affected by the molecular diffusion mechanism since the mass transfer rate is inversely proportional to the pressure. The same dependence on the pressure is observed for the molecular (bulk) diffusion coefficient in the Chapman−Engskog or Fuller equation.[19]

The diffusion mechanism, where the interactions molecule−wall are more frequent than the interactions among molecules, is known as the Knudsen diffusion. From the kinetic theory of gases, the mean free path (λ), the distance a molecule travels between two collisions, is given by the following expression (16):[5]

$$\lambda = \frac{kT}{P\pi d_{\text{molecule}}^2 \sqrt{2}} \qquad (16)$$

Now, if the mean free path is larger than the pore diameter the Knudsen diffusion is the governing mechanism; if the pore diameter is much bigger than λ the bulk diffusion regime dominates. Consequently, a transition from bulk diffusion to Knudsen diffusion is expected as the pressure decreases since the mean free path increases. However, this transition is observed only for diffusion in small pores or for diffusion of larger molecules. If this was the case here, we would expect a different effect of pressure on the slope of a breakthrough curve. The Knudsen diffusion coefficient itself is not a function of pressure, and thus small or no effect would be observed.

The effect of pressure on the adsorption kinetics was studied for both 3.6 and 1.8 mm pellets, and the same trends were observed. It is therefore concluded that the macropores make a significant contribution to the overall mass transfer resistance and that macropore diffusion is controlled by the molecular diffusion mechanism alone.

For desorption runs (see Figure 11) the effect of pressure on the rate of adsorbent regeneration was not as significant as for the adsorption. It seems that the desorption rate might be controlled by other factors such as diffusion in micropores, thermal effects, and isotherm effects.

Effect of Water Concentration. The effect of water partial pressure in the feed stream was studied at temperature 167 °C, pressure 448 kPa, and nitrogen flow rate 15 SLM for two different pellet sizes; see experimental runs w4, w7, w8, w11, w13, and w14. In both cases, water partial pressures studied were 8.2, 12.3, and 16.4 kPa.

The stoichiometric breakthrough time θ_s decreased as the water partial pressure increased; see Figure 12. This was expected because the bed is saturated faster if there is more water in the feed stream. Experimental breakthrough times for 8.2 and 16.4 kPa were approximately 0.65 and 1.2 h, respectively. The corresponding equilibrium loadings q^* were 4.76 and 5.91 mol/kg, respectively. The values of the stoichiometric breakthrough time θ_s were evaluated for experimental runs w4 and w8 to 2.33 and 1.4 h, respectively. As mentioned earlier, θ_s corresponds to a shock breakthrough curve in the absence of any mass transfer resistance; the ratio of $\theta_b/\theta_s = 1$. It follows that the closer the breakthrough time ratio to a unity is the smaller the mass transfer resistance is. By inspection of the experimental and stoichiometric breakthrough times it is evident that the system approaches infinite mass transfer as the feed concentration increases. Hence, it was concluded that, with increasing partial pressures, sharper concentration profiles were observed as a consequence of the favorable isotherm affecting the kinetic parameters. The same information can be obtained from the temperature profiles, where an increase in the water concentration leads to higher and steeper temperature curves.

At the end of adsorption, the desorption step that followed maintained the same operating conditions; see Figure 13. The slow process was due to the fact that desorption was controlled by the unfavorable equilibrium isotherm and the situation got worse as the concentration decreased.

Effect of Carrier Gas Flow Rate. Experimental runs w11 and w15 were designated to show the effect of the carrier gas flow rate on the adsorption and desorption performance. Experimental conditions are summarized in Table 4. Measured concentration and temperature profiles for adsorption runs are depicted in Figure 14. Concentration and temperature profiles for run w15 looked almost identical to those from run w11. An increase of the flow rate had
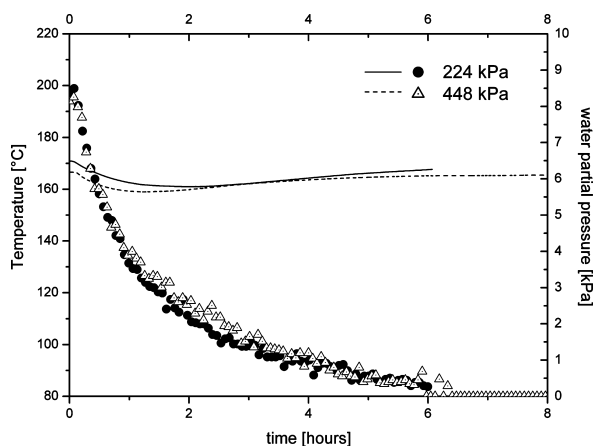
Figure 11. Temperature and concentration profiles for water desorption on 3A zeolite for pressures 224 and 448 kPa, respectively. Temperature at axial position of 2/3L is shown. Pellet size was 3.6 mm.
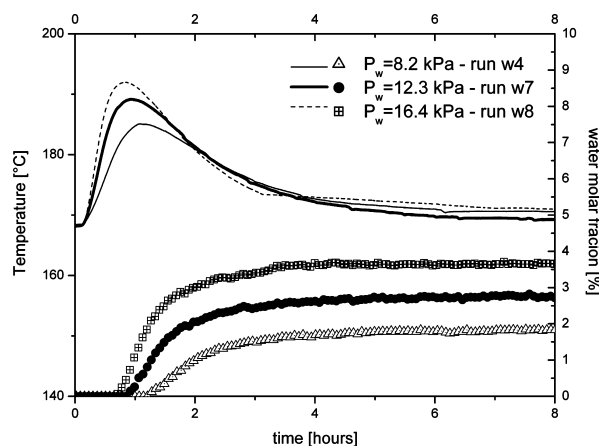

Figure 12. Temperature readings at axial position $z = 2/3L$ and concentration profiles for water partial pressures 8.2, 12.3 and 16.4 kPa, respectively. Experimental conditions for adsorption runs: 167 °C, 448 kPa, 15 SLM N_2 flow, and pellet size 3.6 mm.
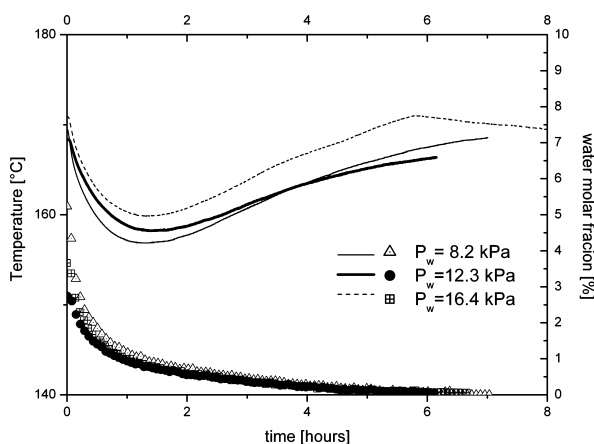

Figure 13. Temperature readings at axial position $z = 2/3L$ and concentration profiles for water partial pressures 8.2, 12.3, and 16.4 kPa, respectively. Experimental conditions for desorption runs: 167 °C, 448 kPa, 15 SLM N_2 flow, and pellet size 3.6 mm.

a positive effect on the film mass transfer and heat transfer coefficients. The Reynolds number increased from 27 to 54. The profiles at a higher flow rate were slightly steeper, suggesting that film resistance was present but its contribution to the overall mass transfer resistance was only minimal.
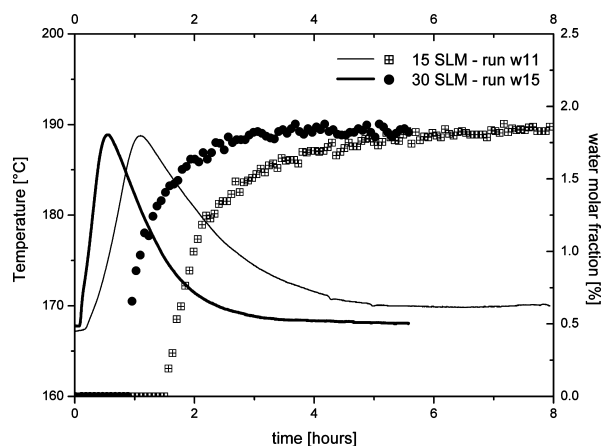

Figure 14. Adsorption runs w11 and w15. Temperature readings at axial position $z = 2/3L$ and concentration profiles for carrier gas flow rate of 15 and 30 SLM, respectively. Experimental conditions: 167 °C, 448 kPa, 8.2 kPa water partial pressure, and pellet size 1.8 mm.
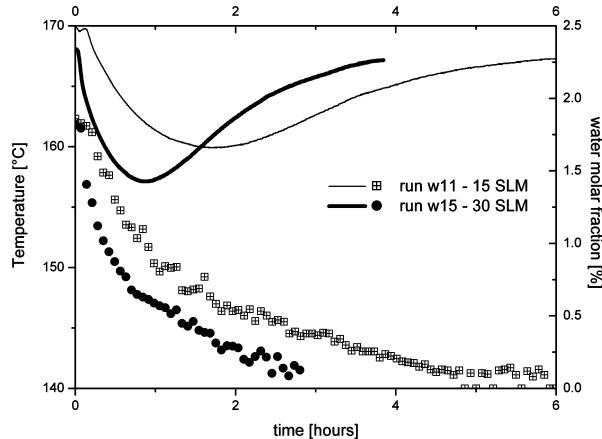

Figure 15. Desorption runs w11 and w15. Temperature readings at axial position $z = 2/3L$ and concentration profiles for carrier gas flow rate of 15 and 30 SLM, respectively. Experimental conditions: 167 °C, 448 kPa, 8.2 kPa water partial pressure, and pellet size 1.8 mm.

The results for desorption runs w11 and w15 are shown in Figure 15. The regeneration time was halved when the flow rate was doubled. The breakthrough time for adsorption with flow rate 15 SLM was less than 2 h; see Figure 14. At the same conditions the regeneration took almost 6 h; however, when the purge flow rate was doubled the regeneration process took only 3 h.

Effect of Particle Size. The size of the pellet affects many system parameters such as film coefficients, dispersion in packed bed, bed porosity, and intraparticle transport processes. The effect of the first three is usually not significant in an industrial adsorber; however, the last one can be detrimental if the macropore diffusion is controlling the mass transfer rate. In other words, the change of the pellet size will have no effect on the breakthrough curve if the macropore diffusion is negligible.

Experimental runs w9 and w15 were designated to address this issue. Concentration and temperature profiles are plotted in Figure 16. The breakthrough times for 3.6 and 1.8 mm pellets were 0.44 and 0.89 h, respectively. This significant improvement of the adsorber performance was due to the fact that the macropore resistance decreased by a factor of 4 since the diffusion time scale for macropores depends on the square of the particle radius. This kinetic effect can be followed from the temperature profiles as well. The temperature peaks were steeper and narrower due to an increase in the mass transfer rate.
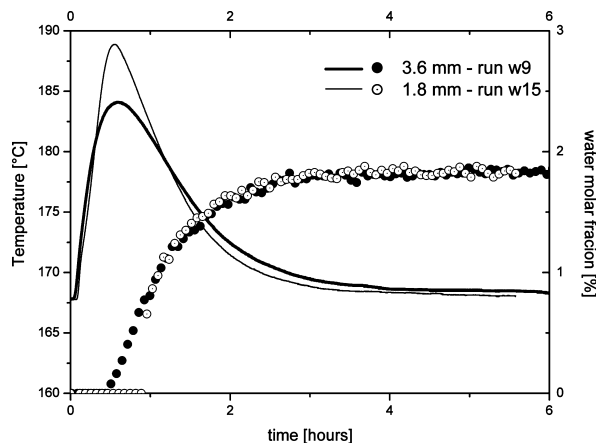
Figure 16. Adsorption runs w9 and w15. Temperature readings at axial position $z = 2/3L$ and concentration profiles for pellet size of 3.6 and 1.8 mm, respectively. Experimental conditions: 167 °C, 448 kPa, 8.2 kPa water partial pressure, and nitrogen flow 30 SLM.
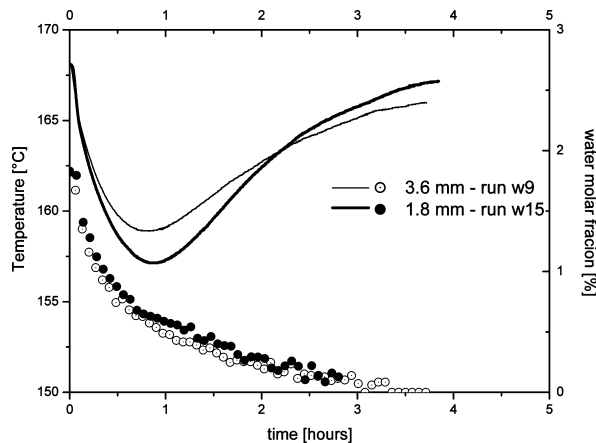

Figure 17. Desorption runs w9 and w15. Temperature readings at axial position $z = 2/3L$ and concentration profiles for pellet size of 3.6 and 1.8 mm, respectively. Experimental conditions: 167 °C, 448 kPa, 8.2 kPa water partial pressure, and nitrogen flow 30 SLM.

The effect of the pellet size on the course of desorption is depicted in Figure 17. Almost identical concentration profiles were obtained. The temperature curves were slightly affected. It seems that the micropore diffusion regime is the dominant one for the desorption process.

Modeling of Water Breakthrough Experiments. An experimental parametric study has investigated the effects of operating parameters on the breakthrough curves, thus giving more insight into the mass transfer mechanism governing the adsorption and desorption processes. It was found that both macropore resistance and micropore resistance were relevant for adsorption with a minor effect of laminar film resistance. For desorption, macropore diffusion seemed to play only a minor role, leaving micropores as the controlling mechanism. These clues provided valuable information in the formulation of the kinetic model.

Heat Transfer in Column Wall. Many nonisothermal breakthrough models tacitly assume that the temperature of the adsorber wall is constant during the course of an experiment. Such an assumption is valid for systems where the adsorber column is not isolated, the column operates at room temperature, and thermal effects are only moderate as for example trace component separations. Otherwise, the heat balance for the adsorber wall is required in the model in order to capture the column dynamics properly.
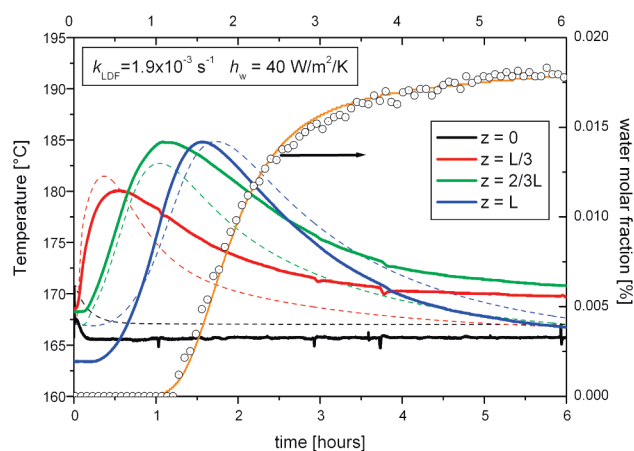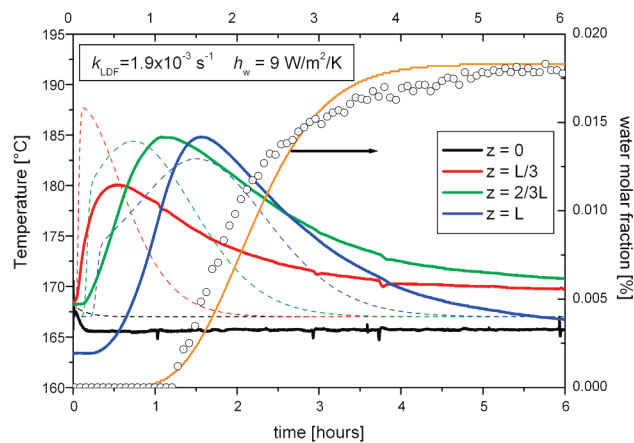

Figure 18. Modeling of effluent and temperature profiles for adsorption run w4 with simplified model considering constant wall temperature (top) and rigorous model (bottom). Full lines correspond to experimental data and dashed lines to predicted data for temperature profiles.

Next, we will compare the quality of the fit for the experimental run w4 for two mathematical models. Figure 18 (top) shows the results for the situation where the wall temperature is considered constant (eq 6 is neglected in the model), and Figure 18 (bottom) depicts the results of the full rigorous model summarized in Table 1.

The correct value of the k_{LDF} coefficient was used in both simulations to show the discrepancies, and the value of h_w was the remaining free parameter. The rigorous model predicted both concentration and temperature curves very well. The temperature of the hot spot increased as the adsorption front progressed down the bed. It is evident that the heat exchange "zeolite bed—adsorber wall" was responsible for these phenomena observed in all performed experiments.

The temperature of the pellet and ambient gas increased upon the exothermic adsorption of water. Only a portion of the generated heat was transferred axially by convection in the bed because of a relatively low volumetric thermal capacity of nitrogen gas. Since the heat capacity of the wall was comparable to the heat capacity of adsorber it acted as a heat sink, so the remaining heat was transferred to the column wall. As a result, the temperature of the wall locally increased and that created a driving force for the axial heat conduction in the wall and radial heat transfer through the insulation to the environment. By comparing the magnitudes of particular terms in eq 6, it was found that the axial conduction in the wall had only a marginal effect. The rate of heat transfer through the insulation was the slowest process. For illustration, the transient bed and wall temperature profiles are plotted in Figure 19.
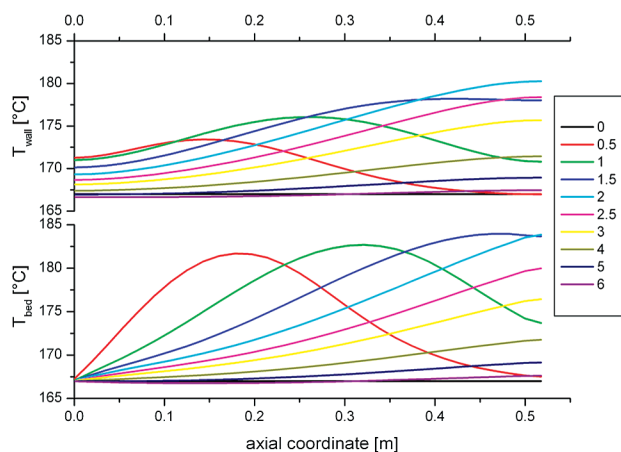
Figure 19. Transient adsorber bed and wall temperature profiles as a function of axial coordinate. Particular time values in hours can be found in the legend. Calculated data correspond to the fit for experimental run w4 depicted in Figure 18, bottom.

Analysis of Overall Mass Transfer Resistance. Experimental adsorption and desorption runs were analyzed with the developed mathematical model and the values of the two remaining parameters—overall mass transfer rate coefficient k_{LDF} and wall heat transfer coefficient h_w—were determined. The values of the wall heat transfer coefficient fell in the range from 30 to 70 $W \cdot m^{-2} \cdot K^{-1}$.

Next, the overall mass transfer resistance was evaluated as the inverse of the k_{LDF} coefficient for all runs. Three mass transfer resistances in series were considered for both adsorption and desorption runs according to general trends observed in the experimental parametric study: external film, macropore region, and micropore region.

The experimental conditions along with the obtained k_{LDF} values are summarized in Table 4. By inspection of the resistance values, it is clear that the contribution of the external film resistance was small (less than 10%). This was expected since the values of Reynolds and Biot numbers were in the ranges 19−101 and 22−51, respectively. According to Do,[24] the external mass transfer mechanism can be neglected for the Biot number larger than 50, and thus we had to include it in our study.

Several studies identified the micropore diffusion as the governing mechanism.[7,8] Our experimental results indicate that the kinetics was dominated by the resistance in both macropores and micropores. The major mechanism responsible for the molecular transport in macropores was the molecular diffusion as was confirmed experimentally by varying the overall pressure and the pellet size. In order to evaluate the macropore resistance, the equation of Fuller et al.[19] was used to evaluate the bulk diffusion coefficient for water−nitrogen mixture and a tortuosity factor of 2 was used according to work by Teo.[6] After evaluating the resistance of the external film and macropores, the resistance in the micropore region could be evaluated using the experimental value of the overall mass transfer resistance; see Table 4.

It was pointed out in the previous section that the contribution of a particular mechanism toward the overall resistance depends on the operating conditions. Trends in the adsorption kinetics for all experiments are summarized in Figure 20. A strong temperature dependence of the k_{LDF} coefficient is evident for experiments w1−w4 carried out at 146, 100, 200, and 167 °C, respectively. At 100 °C more than 60% of the mass transfer resistance was due to the micropore region, while at 200 °C this contribution was negligible. Transition toward the macropore diffusion control was observed as the temperature increased.
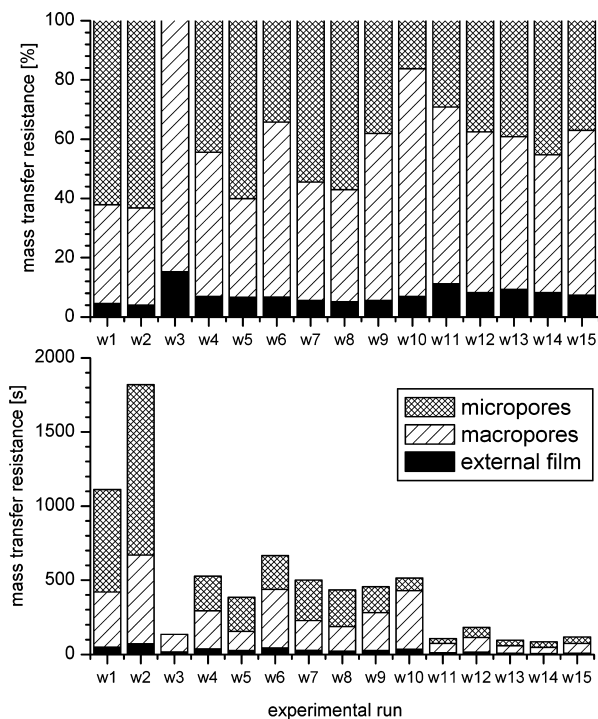

Figure 20. Individual mass transfer resistances for adsorption experiments w1−w15 in percentage of overall resistance (top) and absolute mass transfer resistance values (bottom).

Since the isotherm is more favorable at lower temperatures, sharper breakthrough curves were observed with decreasing temperature as reported by Raghavan for the system "water−4A zeolite" at room temperature.[4] However, the pellet uptake was controlled entirely by macropore diffusion. It follows that at room temperature a sharper water breakthrough will be observed for a 4A zeolite since there is no additional resistance from micropores, which is the governing mechanism in a 3A zeolite at a low temperature. Consequently, a 4A zeolite is the preferred adsorbent for air drying applications.

The effect of pressure on the mass transfer resistance was studied in runs w4, w5, and w6 performed at 448, 224, and 689 kPa, respectively. At lower pressures, micropore diffusion controlled the pellet uptake. Approximately 60% of the resistance was in the micropore region. On the other hand, for higher pressures, micropores were responsible for less than 30% of the overall resistance; see run w6 in Figure 20. Transition toward the macropore diffusion control was observed as the pressure increased.

Experimental runs w10, w4, w7, and w8 were designated to show the effect of the water concentration. By comparing conditions in experiments w10, w4, w7, and w8, the corresponding water partial pressures were 3.11, 8.2, 12.3, and 16.4 kPa and the equilibrium solid phase loadings were 2.91, 4.76, 5.47, and 5.9 mol/kg, respectively. As a result, the overall mass transfer coefficients increased with the increasing water concentration. Figure 20 shows that the contribution of the macropore resistance decreased (76%, 48%, 40%, and 37%) while the contribution of the micropore resistance increased (16%, 44%, 54% and 57%) as the water concentration increased. These opposite trends can be interpreted by lower values of the partition coefficient Λ as the water concentration increased; i.e., the macropore resistance is smaller. Diffusion in micropores was actually faster at higher concentrations; however, since both mechanisms were present the decrease in partition ratio had a stronger effect. Generally, transition toward the micropore diffusion control was observed as the concentration increased.
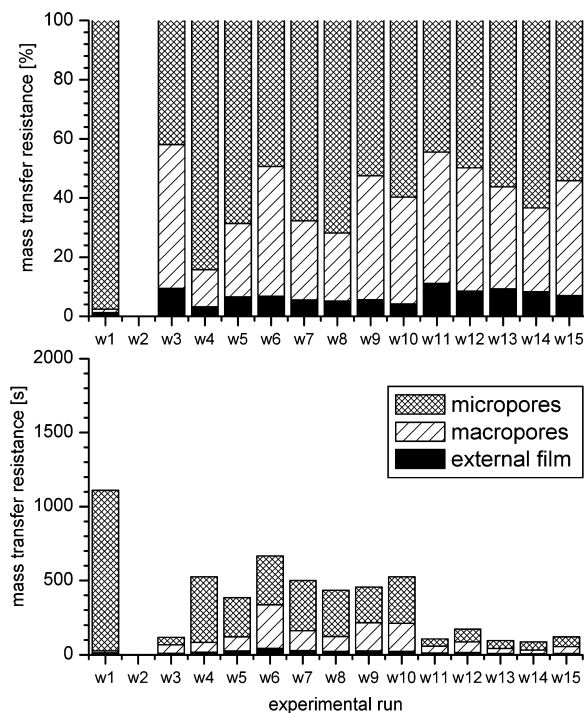
Figure 21. Individual mass transfer resistances for desorption experiments w1−w15 in percentage of overall resistance (top) and absolute mass transfer resistance values (bottom).

Experimental runs w11−w15 were performed with smaller pellets. The higher k_{LDF} values can be explained through the quadratic dependence of the macropore resistance on the particle radius; approximately 4 times smaller resistance was observed. The situation in micropores also unexpectedly improved. Since both zeolites were from the same manufacturer the diffusion coefficients should be similar; however, it is possible that smaller pellets were prepared from smaller crystals, accounting for 4-fold decrease in the micropore resistance as well.

The mass transfer resistance summary for desorption runs is depicted in Figure 21. Overall, the k_{LDF} values are similar to those obtained for adsorption; however, the relative contributions of macropore resistance and micropore resistance seem to be shifted toward the micropore control. The observed trend can be explained by the effect of an unfavorable isotherm for desorption affecting the micropore diffusion coefficient through the concentration dependent term in the Darken equation. This also explains why the change of the particle size and pressure did not have any significant effect on the course of desorption step, i.e., lower contribution of macropores toward the overall mass transfer resistance. The trends in the concentration and pellet size follow the explanation stated above for adsorption. The sole micropore control was observed for low temperature run w1 while at high temperature both mechanisms contribute equally.

Water Adsorption and Desorption Kinetics Model. The experimental values for the resistance in micropores could be used to directly evaluate the crystal diffusion coefficient and the self-diffusion coefficient. The problem is the proper integral value of the concentration dependent term in the Darken equation relating these two diffusivities.

The experimental data were fitted again utilizing eqs 9 and 10 to obtain the values of D_0/r_c^2 at different temperatures directly instead of estimating the lumped k_{LDF} parameter. A satisfactory fit was obtained by using the same value of corrected diffusivity for both adsorption and desorption; see Table 5. The temperature dependence of corrected diffusivity is usually correlated by the

Table 5. Corrected Diffusion Coefficients

T [°C]	$10^3(1/T)$ [K^{-1}]	D_0/r_c^2 [s^{-1}]	$\ln(D_0/r_c^2)$
100	2.68	3.5×10^{-5}	−10.26
146	2.39	7×10^{-5}	−9.57
167	2.27	1.5×10^{-4}	−8.80

Arrhenius dependence. A linear plot of $\ln D_0/r_c^2$ vs $1/T$ was used to estimate the activation energy for diffusion of water in a zeolite crystal. The experiment performed at 200 °C was not included since the contribution of micropore resistance was negligible. The value of the activation energy E_a was 27.6 kJ/mol, and the diffusion coefficient at infinite temperature divided by r_c^2, D_0^∞/r_0^2, extrapolated to 0.2553 s^{-1}. For experiments with smaller pellets D_0/r_c^2 equals 8.5×10^{-4} s^{-1} measured at 167 °C, which was approximately 4 times higher than the corresponding value for larger pellets.

Diffusion in zeolites was widely studied.[5] While different zeolite samples of the same zeolite often show large differences in diffusivities, there is generally little variation in the activation energy. The activation energies correlate very well with the molecular size. A significant amount of diffusivity data is available in the literature for A-type zeolites.[5] Typical values of the activation energy fall in the range from 19 to 60 kJ/mol. Tian et al. reported an activation energy of 30.2 kJ/mol.[9] They measured the micropore diffusion coefficients for water on a 3A zeolite directly by using gravimetric temperature programmed desorption experiments. Their value is in excellent agreement with our result, taking into account the fact that entirely different techniques were used.

Conclusions

The pilot scale near-adiabatic fixed bed apparatus was designed and constructed to investigate the water and ethanol adsorption behaviors on a W. R. Grace 3A zeolite. Adsorption breakthrough experiments were used to study both equilibrium and kinetics in the range relevant to the operating conditions of a commercial ethanol−water PSA process.

Water equilibrium data conformed to the Langmuir isotherm model with the temperature dependent saturation capacity. A very low ethanol uptake of 0.03 mol/kg was observed at 167 °C. The value of the adsorbent selectivity for "ethanol−water" PSA process feed stream conditions was evaluated to be ≈900. The adsorbent selectivity is analogous to the relative volatility in distillation; hence, a very high value of selectivity demonstrates the molecular sieving mechanism for this separation process.

The adsorption−desorption kinetics study investigated the effects of the pressure, temperature, water concentration, bed velocity, and pellet size on the shape of the breakthrough curves to identify the relevant mass transfer mechanisms. Strong temperature dependence was revealed; the slope of the breakthrough curves increased with the increasing temperature, thus confirming the activated micropore diffusion mechanism. The experiments at different pressures and pellet sizes identified that the macropore diffusion mechanism had a considerable effect as well. The gas velocity had only a weak effect on the breakthrough curves since the experiments were performed at high Reynolds numbers. As a result, three resistances in the series model were proposed to describe the adsorption and desorption kinetics of water on a 3A zeolite.

It was observed that mass transfer was controlled by the diffusion in micropores as the pressure decreased and the water concentration increased; on the other hand, transition to the macropore diffusion mechanism was observed for experiments at higher temperatures. Approximately 60% of the overall mass

transfer resistance was in the micropore region for desorption, while for adsorption this contribution was close to 40%. It is obvious that the effect of the isotherm nonlinearity was more pronounced during desorption through the concentration dependence of the micropore diffusion coefficient. Hence, the fact that the isotherm was unfavorable for desorption further explains the slow regeneration process of a 3A zeolite.

The proposed kinetic model was used as an input to a mathematical model developed for the analysis of the dynamic column response. The axially dispersed plug flow model accounted for the variation of axial bed velocity. Heat effects had a significant effect on the column performance because of the high heat of adsorption and near-adiabatic operation of the laboratory column. A detailed heat transfer model had to consider the energy balance for a gas phase, solid phase, and bed wall in order to reproduce the measured temperature profiles. A mathematical model was employed to estimate the micropore diffusion coefficients. The Darken equation was used to account for the temperature and concentration dependence of micropore diffusivity. The activation energy for water diffusion in W. R. Grace 562ET zeolite crystal was evaluated to be 27.6 kJ/mol.

All experimental profiles measured in the range of pressures from 224 to 689 kPa and temperatures 100−200 °C were successfully reproduced using the proposed adsorption−desorption kinetic model comprised of the following mass transfer mechanisms: external film, molecular diffusion in macropores, and micropore diffusion in zeolite crystals. The formulated kinetic model will be used to study a commercial ethanol dehydration PSA process.

Acknowledgment

Notation

b = isotherm equilibrium constant (adsorption affinity) [Pa^{-1}]
c = fluid phase molar concentration [mol·m^{-3}]
c_p = isobaric specific heat [J·kg^{-1}·K^{-1}]
D, D_1 = internal bed diameter [m]
D_2, D_3 = outer bed diameter, external bed diameter including insulation [m]
D_c = micropore (zeolite crystal) diffusion coefficient [m^2·s^{-1}]
D_0^∞ = corrected diffusion coefficient at infinite temperature [m^2·s^{-1}]
D_{eff} = effective diffusion coefficient ($=\varepsilon_P D_p/\tau$) [m^2·s^{-1}]
D_L = axial effective dispersion coefficient [m^2·s^{-1}]
D_M = molecular (bulk) diffusion coefficient [m^2·s^{-1}]
d_P = pellet diameter [m]
D_P = macropore diffusion coefficient [m^2·s^{-1}]
E_a = activation energy for diffusion in zeolite crystal [J/mol]
F = volumetric or mass flow rate [SLM] or [g/h]
h_e = external heat transfer coefficient [W·m^{-2}·K^{-1}]
h_{fs} = fluid−solid heat transfer coefficient [W·m^{-2}·K^{-1}]
h_w = heat transfer coefficient at the bed wall [W·m^{-2}·K^{-1}]
k = Boltzmann constant ($=1.38 \times 10^{-23}$ J·K^{-1})
k_f = external/fluid mass transfer coefficient [m·s^{-1}]
k_{LDF} = linear driving force (overall) mass transfer coefficient [s^{-1}]
m_z = amount of adsorbent (zeolite) in packed bed [kg]
P = pressure [Pa]
q^* = equilibrium sorption capacity [mol·kg^{-1}]
q_s = saturation loading capacity [mol·kg^{-1}]
$\bar{q}$ = volume averaged pellet adsorbate loading, $\bar{q} = (3/R^3)\int_0^R q(r)\, r^2\, dr$ [mol·kg^{-1}]
Q_L = band heater power output per unit bed length [W·m^{-1}]

Q_{st} = isosteric heat of adsorption ($= -\Delta H_{st}$) [J·mol^{-1}]
R = universal gas constant [J·mol^{-1}·K^{-1}]
r_c = zeolite crystal radius [m]
R_P = adsorbent particle (pellet) radius [m]
t = time variable [s]
T = temperature [K]
u_s = superficial velocity [m·s^{-1}]
Y = fluid phase molar fraction
z = bed spatial coordinate [m]

Dimensionless Parameters

Bi_f = fluid phase Biot mass transfer number ($=k_f R_P/\varepsilon_P D_p$)
Nu = Nusselt number ($=hd_P/\lambda_g$)
Pe_{AF} = axial fluid phase Peclet number ($=u_s\rho_g c_{p,g}d_P/\lambda_L$)
Pr = Prandtl number ($=c_{p,g}\mu_g/\lambda_g$)
Re_P = particle Reynolds number ($=u_s d_P\rho_g/\mu_g$)
Sc = Schmidt number ($=\mu_g/\rho_g D_M$)
Sh = Sherwood number ($=k_f d_P/D_M$)

Greek Symbols

Λ = partition ratio
ε = void fraction
λ = molecule mean free path [m]
λ_L = axial thermal conductivity of the fluid [W·m^{-2}·K^{-1}]
λ_w = thermal conductivity of bed wall [W·m^{-1}·K^{-1}]
μ = viscosity [Pa·s]
θ_s = stoichiometric (shock front) breakthrough time ($=m_z q_{ref}/F_{feed}$) [s]
ρ = density [kg·m^{-3}]
τ = tortuosity

Subscripts

B = bulk or bed
c = zeolite crystal
F = feed (inlet) conditions
g = gas (fluid) phase
P = particle, pellet
ref = reference conditions (usually feed stream)
s = solid (adsorbed) phase
w = wall

Literature Cited

(1) Katzen, R.; Moon, G. D., Jr.; Kumana, J. D. Distillation method and apparatus for making motor fuel grade anhydrous ethanol. EP 11147, 1980.

(2) Tindall, B. M.; Natarajan, R. S. Production of anhydrous ethanol by pressure swing adsorption. In AIChE: New York, NY, Minneapolis, MN, 1987.

(3) Malek, A.; Farooq, S. Kinetics of hydrocarbon adsorption on activated carbon and silica gel. *AIChE J.* **1997**, *43* (3), 761–776.

(4) Raghavan, N. S.; Ruthven, D. M. Dynamic behavior of an adiabatic adsorption column−II. Numerical simulation and analysis of experimental data. *Chem. Eng. Sci.* **1984**, *39* (7−8), 1201–1212.

(5) Karger, J.; Ruthven, D. M. *Diffusion in Zeolites: and Other Microporous Solids*; Wiley-Interscience: New York, 1992.

(6) Teo, W. K.; Ruthven, D. M. Adsorption of water from aqueous ethanol using 3-Å molecular sieves. *Ind. Eng. Chem. Process Des. Dev.* **1986**, *25* (1), 17–21.

(7) Kupiec, K.; Rakoczy, J.; Mirek, R.; Georgiou, A.; Zielinski, L. Determination and analysis of experimental breakthrough curves for ethanol dehydration by vapor adsorption on zeolites. *Inz. Chem. Proces.* **2003**, *24* (2), 293–310.

(8) Sowerby, B.; Crittenden, B. D. A vapor-phase adsorption and desorption model for drying the ethanol-water azeotrope in small columns. *Chem. Eng. Res. Des.* **1991**, *69* (A1), 3–13.

(9) Tian, Y.; Zhang, M.; Dong, X. Adsorption and diffusion equilibrium of water on 3A molecular sieve. *Shiyou Huagong* **2004**, *33* (10), 932–936.

(10) Gorbach, A.; Stegmaier, M.; Eigenberger, G. Measurement and Modeling of Water Vapor Adsorption on Zeolite 4A-Equilibria and Kinetics. *Adsorption* **2004**, *10* (1), 29–46.

(11) Ruthven, D. M. *Principles of Adsorption and Adsorption Processes*; Wiley-Interscience: New York, 1984.

(12) Simo, M.; Brown, C. J.; Hlavacek, V. Simulation of pressure swing adsorption in fuel ethanol production process. *Comput. Chem. Eng.* **2008**, *32* (7), 1635–1649.

(13) Glueckauf, E.; Coates, J. E. Theory of chromatography. *J. Chem. Soc.* **1947**, 1315.

(14) Sircar, S.; Hufton, J. R. Why Does the Linear Driving Force Model for Adsorption Kinetics Work. *Adsorption* **2000**, *6*, 137–147.

(15) Schiesser, W. E. *The Numerical Method of Lines*, 1st ed.; Academic Press: San Diego, CA, 1991.

(16) Petzold, L. A description of DASSL: a differential algebraic system solver. In *IMACS Trans. Scientific Computing Vol. 1*; Stepleman, R. S., Ed.; North-Holland: Amsterdam, 1993; pp 65−68.

(17) Dixon, A. G.; Cresswell, D. L. Theoretical prediction of effective heat transfer parameters in packed beds. *AIChE J.* **1979**, *25* (4), 663–676.

(18) Wakao, N.; Funazkri, T. Effect of fluid dispersion coefficients on particle-to-fluid mass transfer coefficients in packed beds. Correlation of Sherwood numbers. *Chem. Eng. Sci.* **1978**, *33* (10), 1375–1384.

(19) Reid, R. C.; Prausnitz, J. M.; Poling, B. E. *Properties of Gases and Liquids*, 4th ed.; McGraw-Hill: New York, 1987.

(20) Carmo, M. J.; Gubulin, J. C. Ethanol-water adsorption on commercial 3A zeolites: kinetic and thermodynamic data. *Braz. J. Chem. Eng.* **1997**, *14* (3), 217–224.

(21) Lalik, E.; Mirek, R.; Rakoczy, J.; Groszek, A. Microcalorimetric study of sorption of water and ethanol in zeolites 3A and 5A. *Catal. Today* **2006**, *114* (2−3), 242–247.

(22) Ruthven, D. M.; Farooq, S.; Knaebel, K. S. *Pressure Swing Adsorption*; VCH Publishers, Inc.: New York, 1994.

(23) Silva, J. A. C.; Rodrigues, A. E. Fixed-Bed Adsorption of n-Pentane/Isopentane Mixtures in Pellets of 5A Zeolite. *Ind. Eng. Chem. Res.* **1997**, *36* (9), 3769–3777.

(24) Do, D. D. Analysis of Adsorption Kinetics in a Zeolite Particle. In *Adsorption Analysis: Equilibria and Kinetics*; Imperial College Press: London, 1998.